Doping Location-Dependent Energy Transfer Dynamics in Mn-Doped CdS/ZnS Nanocrystals

Hsiang-Yun Chen, Sourav Maiti, and Dong Hee Son*

Department of Chemistry, Texas A&M University, College Station, Texas 77842, United States

ABSTRACT

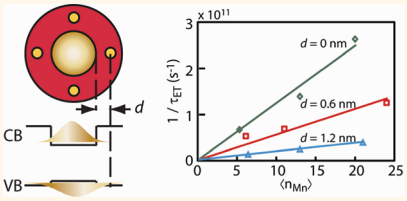

Dynamics of energy transfer and charge carrier localization in Mn-doped CdS/ZnS core/shell nanocrystals correlated with doping location and concentration are studied *via* transient absorption measurement of exciton relaxation dynamics. The strong dependence of exciton—Mn energy transfer rate on doping location was directly resolved in the transient bleach recovery and electron intraband absorption data by using layer-by-layer synthesized Mn-doped nanocrystals. With 1.2 nm decrease in doping radius in the ZnS shell, energy transfer rate increases by 6 fold. We identified that hole trapping is the major competing process that inhibits the energy transfer in Mn-doped CdS/ZnS nanocrystals. From the branching ratio of the energy transfer and hole trapping, combined with luminescence quantum yield measurement, we also obtained doping location-dependent radiative relaxation quantum yield of Mn^{2+} ions that is as high as 0.95.

KEYWORDS: doped semiconductor nanocrystals · energy transfer · transient absorption · luminescence quantum yield · exciton dynamics

Doping of semiconductor nanocrystals is attracting significant attention as a way to introduce new optical, electronic, and magnetic properties originating from the dopant ions interacting with charge carriers of the semiconductor host in the confined space of the nanocrystals.[1−3] In particular, semiconductor nanocrystals doped with transition metal ions have shown interesting luminescence and magnetic properties applicable in optoelectronics and spintronics.[4−7] Because of the spatially confined nature of the nanocrystals, the interaction of the dopant ions with charge carriers responsible for many new properties of doped nanocrystals is stronger than in their bulk counterparts, leading to the enhancement of the dopant-related material properties.[2,3] For instance, Mn phosphorescence and photoinduced ferromagnetism in Mn-doped CdS or CdSe nanocrystals, resulting from exciton—Mn energy transfer and formation of excitonic magnetic polaron, respectively, are stronger due to the greater overlap of the exciton and dopant wave functions than in the bulk.[2,8,9]

The strength of exchange coupling between the dopant and charge carriers that dictates the rate of many interesting photophysical processes in doped semiconductor nanocrystals depends on the wave function overlap of exciton and dopant ions.[10,11] Trapping of the charge carriers by the structural defect and new trap states that can potentially be introduced by doping, in addition to the preexisting trap states, also depends on the electronic coupling of "donor" and "acceptor" sensitive to the doping location and concentration.[12] Therefore, the dynamics of photophysical processes of doped semiconductor nanocrystals, including exciton relaxation and energy transfer, will be strongly affected by the spatial location and concentration of dopant within the nanocrystals.

However, studying the dynamics of the photophysical processes in doped semiconductor nanocrystals correlated with the doping location has been challenging partly due to the difficulties in obtaining doped nanocrystals with well-defined doping location and the added complexity in the dynamics. In the majority of the syntheses of doped semiconductor nanocrystals, the radial doping location in the nanocrystals was either random or poorly controlled.[13−15] Dynamics measured from an ensemble of such nanocrystals will be highly heterogeneous and information on the doping location dependence will be buried under the structural heterogeneity. So far, only a small number of studies have addressed the properties of doped nanocrystals correlated

* Address correspondence to dhson@mail.chem.tamu.edu.

Received for review October 13, 2011 and accepted December 18, 2011.

Published online December 18, 2011
10.1021/nn204452e

with doping location, mostly on the dopant luminescence and its quantum yield in Mn-doped II–VI semiconductor nanocrystals.[16,17]

In this study, we investigated the dynamics of exciton relaxation and exciton–Mn energy transfer in Mn-doped CdS/ZnS core/shell nanocrystals correlated with the radial doping location and doping concentration *via* pump–probe transient absorption measurements. For this purpose, we employed a layer-by-layer synthesis method to prepare the spherical doped nanocrystals with the largely removed heterogeneity in the radial doping location.[18] The exciton dynamics in Mn-doped nanocrystals reflects the competition among many processes such as exciton recombination, charge carrier trapping and exciton–Mn energy transfer processes.[19–22] From the measurements of transient absorption at the band-edge and near-infrared regions, structurally correlated rates of exciton–Mn energy transfer and competing charge carrier trapping process were obtained. The rate of exciton–Mn energy transfer was strongly dependent on doping location, showing ~6 fold increase with 1.2 nm decrease in doping radius in ZnS shell in this study. Hole trapping, occurring on a 50–100 ps time scale, was identified as the major nonradiative pathway competing with exciton–Mn energy transfer. In addition, the quantum yield of radiative relaxation of the Mn excited state also exhibited dependence on the doping location and concentration, which can become close to unity. Information on the structurally resolved dynamics of various photophysical processes in Mn-doped nanocrystals in this study will provide a valuable insight into the structural control of the properties of doped semiconductor nanocrystals.

RESULTS AND DISCUSSION

Two different pairs of undoped and Mn-doped spherical core/shell nanocrystals were synthesized in this study using CdS/ZnS and CdSe/ZnS core/shell structures as the host nanocrystals. Mn-doped CdS/ZnS nanocrystals were used to investigate the doping radius- and concentration-dependent exciton dynamics in the presence of exciton–Mn energy transfer process. Mn-doped CdSe/ZnS nanocrystals were used to examine the potential role of Mn^{2+} ions as the charge carrier trap since exciton–Mn energy transfer pathway can be blocked by decreasing the bandgap of the host nanocrystals.[11,23] Both doped and undoped core/shell nanocrystals were prepared *via* layer-by-layer coating of the shell on the premade core nanocrystals similar to our earlier work.[24]

Figure 1 displays the representative transmission electron micrograph (TEM) and schematic diagram of the doping location of the Mn-doped CdS/ZnS core/shell nanocrystals used in this study. The nanocrystals have the average core and total diameter of 3.6 and 7.2 nm, respectively. Mn^{2+} ions are doped at three

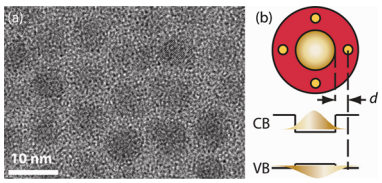

Figure 1. (a) TEM of typical Mn-doped CdS/ZnS nanocrystals. (b) Schematic diagram of the structure of the Mn-doped CdS/ZnS nanocrystals and exciton wave function distribution; *d* is the radial doping location of Mn^{2+} ions (yellow dots). VB and CB are valence and conduction band.

TABLE 1. Exciton (Φ_{ex}) and Mn (Φ_{Mn}) Luminescence Quantum Yield and Mn Luminescence Lifetime (τ_{Mn}) of Doped CdS/ZnS Nanocrystals of Varying Doping Location (*d*) and Concentration ($\langle n_{Mn} \rangle$)

sample	*d* (nm)	$\langle n_{Mn} \rangle$	Φ_{ex}	Φ_{Mn}	τ_{Mn} (ms)	ϕ_{Mn}[a]	$\tau_{Mn}/\tau_{Mn,r}$[b]
undoped		0	0.35				
a1	0	5.3	0.02	0.70	5.2	0.86	0.83
a2	0	13	0.01	0.71	4.6	0.80	0.73
a3	0	20	0.00	0.50	3.3	0.56	0.52
b1	0.6	6.1	0.01	0.76	6.0	0.95	0.95
b2	0.6	11	0.01	0.75	5.8	0.87	0.92
b3	0.6	24	0.00	0.71	4.0	0.79	0.63
c1	1.2	6.4	0.04	0.41	5.1	0.72	0.81
c2	1.2	13	0.02	0.41	4.8	0.68	0.76
c3	1.2	21	0.01	0.46	3.3	0.56	0.52

[a] ϕ_{Mn} is the radiative relaxation quantum yield of Mn obtained from Φ_{Mn} and relative efficiency of energy transfer (f_{ET}). [b] The ratio between the measured τ_{Mn} and the hypothetical radiative lifetime of $\tau_{Mn,r}$ = 6.3 ms. See the text.

different radial locations in the ZnS shell with average distance *d* of 0, 0.6, and 1.2 nm from the interface of core and shell. A detailed discussion on the determination of the average doping location is made in the Supporting Information. For each doping location *d* (labeled as **a**, **b**, and **c**), nanocrystals in three different ranges of doping concentration (labeled as **1**, **2**, and **3**) were prepared as summarized in Table 1. The three different doping concentration groups have average doping concentration of $\langle n_{Mn} \rangle$ = ~6, ~12, and ~22 ions per nanocrystal on average. The diameters of the core and core/shell nanocrystals were obtained from TEM. The average Mn doping concentration was measured from elemental analysis employing inductively coupled plasma mass spectrometry and the particle size was determined from TEM.

Figure 2 shows the absorption and photoluminescence spectra of undoped and three Mn-doped CdS/ZnS nanocrystals with $\langle n_{Mn} \rangle$ = ~6 at various radial doping locations. Both undoped and Mn-doped nanocrystals exhibit very similar absorption spectra, supporting that the core size and shell thickness are nearly identical in all the samples. Undoped nanocrystals show that exciton fluorescence peaked at 433 nm. In Mn-doped nanocrystals, exciton fluorescence was

nearly quenched while the sensitized Mn phosphorescence appeared at ~600 nm arising from the dipole-forbidden ligand field transition ($^4T_1 \rightarrow {}^6A_1$) following exciton–Mn energy transfer.[2,25] Mn phosphorescence emission blue shifts as Mn^{2+} ions are doped closer to the surface of the nanocrystals. This was previously explained by the difference in the local pressure at a different radial doping location resulting from the lattice mismatch at the core/shell interface.[17] The luminescence quantum yields of both exciton (Φ_{ex}) and Mn (Φ_{Mn}) and lifetimes of Mn luminescence (τ_{Mn}) from Mn-doped nanocrystals are shown in Table 1.

To investigate the doping location-dependent exciton relaxation and energy transfer dynamics in undoped and Mn-doped CdS/ZnS nanocrystals, a pump–probe transient absorption (ΔOD) measurement was made on colloidal solutions of the nanocrystals. The bleach recovery at 420 nm and the decay of induced absorption at 880 nm were measured as shown in panels a–c and d–f of Figure 3, respectively. Each panel compares the ΔOD data of the nanocrystal samples with different doping location but in the same doping concentration group. At the probe wavelength of 420 nm, corresponding to the interband transition at the peak of the first excitonic absorption, ΔOD data reflects primarily the electron dynamics. In undoped nanocrystals, it represents the combined dynamics of the radiative recombination of exciton and removal of the electron population from the conduction band by electron trapping as depicted in Figure 4.[19–21,26,27] In Mn-doped nanocrystals, the bleach recovery has an additional contribution from exciton–Mn energy transfer. However, the hole dynamics, such as hole trapping, has little spectroscopic signature at this wavelength in both undoped and doped nanocrystals.[19,20] In some cases, the dopant can also function as the electron or hole trap. However, substitutionally doped Mn^{2+} ions in CdS/ZnS host function as energy acceptors rather than charge carrier acceptors because the charge transfer between a Mn^{2+} ion and valence or conduction band is energetically more expensive than the bandgap transition.[5]

The induced absorption probed at 880 nm exhibits the dynamics that is nearly a mirror image of the bleach recovery measured at 420 nm, although the amplitude is ~50 times smaller. The similarity of the dynamics

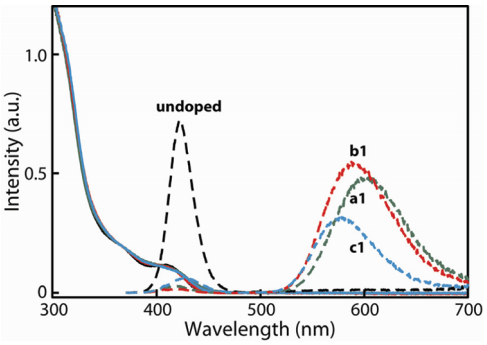

Figure 2. Absorption (solid line) and photoluminescence (dashed line) spectra of undoped (black line) and Mn-doped CdS/ZnS nanocrystals with different doping location (*d*) with $\langle n_{Mn} \rangle$ = ~6. Green, red, cyan are for *d* = 0, 0.6, 1.2 nm, respectively.

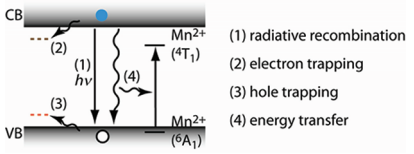

Figure 4. Photophysical processes following the excitation of exciton in Mn-doped semiconductor nanocrystals. CB and VB are conduction and valence band. Dashed lines within the gap represent trap states.

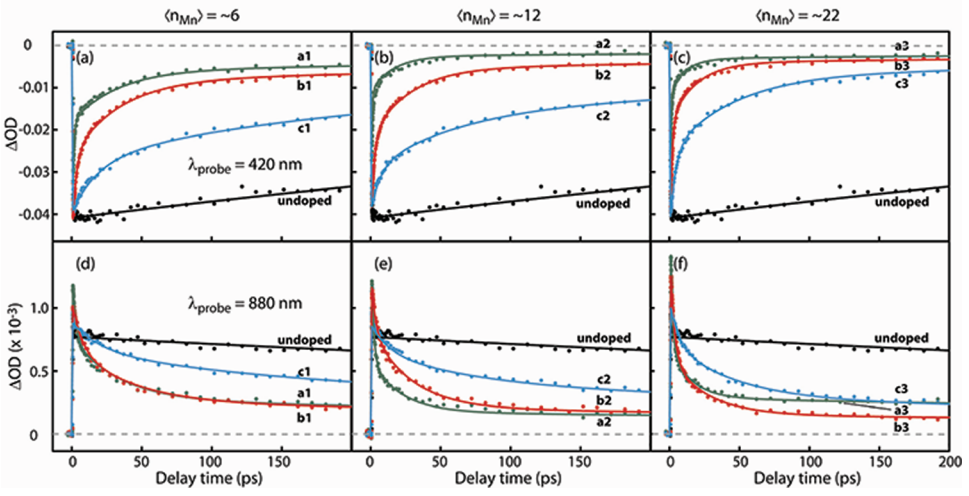

Figure 3. (a–c) Bleach recovery probed at 420 nm and (d–f) induced absorption probed at 880 nm of undoped (black) and Mn-doped CdS/ZnS nanocrystals of varying doping locations and densities. Doping location *d* = 0, 0.6, 1.2 nm for green, red, and cyan curves, respectively. Each panel compares the samples belonging to the same doping concentration group as noted on top of each column.

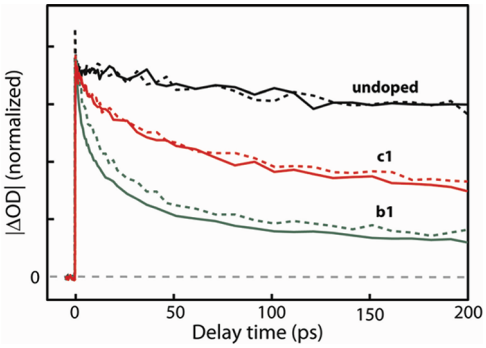

Figure 5. Comparison of the normalized |ΔOD| data probed at 420 (solid line) and 880 nm (dashed line). Undoped nanocrystal (black line), sample b1 (green line), sample c1 (red line).

represented in the data at both probe wavelengths is clearly seen in Figure 5, where the normalized |ΔOD| are compared. In our previous study, we ascribed the induced absorption at 880 nm observed in a similar Mn-doped nanocrystal sample to the intraband absorption of the electrons mixed with absorption from the trapped exciton, although its nature (*i.e.*, electron *vs* hole trap) was not clearly identified.[24] Therefore, |ΔOD| data at these two probe wavelengths contain similar information on the electron dynamics at low initial exciton densities (*e.g.*, <1 exciton/particle), although they become increasingly dissimilar at higher excitation densities due to the saturation of the bleach.[28−30] ΔOD data from all the Mn-doped nanocrystal samples at both probe wavelengths share the following common general features. They exhibit the dynamics occurring on two clearly separated time scales. The fast component, with a few to tens of ps dynamics, becomes faster with increasing doping concentration and smaller value of *d*. The slower component has ~1 ns time constant and does not exhibit noticeable dependence on the doping concentration or location.

We first discuss the bleach recovery data probed at 420 nm in Figure 3a−c. To extract the time scale of the dynamics, we fit the data to the sum of three exponential functions, $-\Sigma r_i \exp(-t/\tau_i)$. The data with an extended time window (750 ps) and the overlaid fit result are also provided in Figure S4 of Supporting Information. The fitting parameters are summarized in Table 2, where r_i is the relative amplitude of the exponential function with time constant τ_i. The fast component in the dynamics was fit with two exponential functions with time constants τ_1 and τ_2. The slow component was fit with a fixed single exponential time constant of 1 ns. The fast component represented by the average time constant $\tau_{avg} = (r_1\tau_1 + r_2\tau_2)/(r_1 + r_2)$ can be assigned to exciton−Mn energy transfer that depletes both the electron and hole population. A single exponential function did not fit the fast component very well, especially for the doped nanocrystals with $d = 0$. This is probably due to the remaining

TABLE 2. Multiexponential Fitting Parameters of ΔOD Data Probed at 420 nm to $-\Sigma r_i \exp(-t/\tau_i)$

sample	r_1	r_2	r_3[a]	τ_1 (ps)	τ_2 (ps)	τ_{avg} (ps)[b]	τ_{tr} (ps)[c]
a1	0.44	0.37	0.18	0.88	32	15	67
a2	0.52	0.37	0.12	0.63	16	7.2	55
a3	0.62	0.27	0.11	0.56	12	3.8	30
b1	0.36	0.44	0.20	2.5	33	19	77
b2	0.44	0.42	0.14	2.1	27	15	89
b3	0.54	0.36	0.10	1.3	18	8.0	70
c1	0.28	0.29	0.43	18	141	80	106
c2	0.23	0.38	0.39	6.6	63	42	64
c3	0.38	0.45	0.17	3.8	45	26	125

[a] r_3 is the amplitudes for τ_3 fixed at 1 ns. [b] $\tau_{avg} = (r_1\tau_1 + r_2\tau_2)/(r_1 + r_2)$. [c] $\tau_{tr} = 1/(f_{tr}(\tau_{tr}^{-1} + \tau_{ET}^{-1}))$.

distribution of the actual doping radius, since the core is not a perfect sphere. Statistical distribution of the doping concentration may also have contributed to the departure from the single exponential kinetics. The slow component, exhibiting essentially the same dynamics as that of undoped nanocrystals, can be interpreted in different ways. One interpretation is the presence of undoped nanocrystals within the ensemble of nanocrystals, resulting in the heterogeneous kinetics, similar to the observation made in quantum dot-dye Förster resonance energy transfer (FRET) pairs with a low surface density of dyes.[27] However, we ruled out this possibility for the following reasons. First, the fraction of undoped nanocrystals in the ensemble of nanocrystals should be <1% in all of our samples, if the doping concentration follows Poisson statistics. The small remaining exciton fluorescence results from the competition between radiative exciton relaxation and other processes, not from the undoped nanocrystals.

Second, the amplitude of the slow-recovery component (r_3) varies largely with the doping location for a given doping concentration, indicating that the slow dynamics is not associated with undoped nanocrystals.

The alternative explanation involves the charge carrier trapping, more specifically hole trapping, which inhibits exciton−Mn energy transfer while not influencing the electron dynamics probed at the band-edge. The effect of hole trapping on the electron dynamics explains very well the observed ΔOD data probed at 420 nm as follows, although the hole trapping itself is spectroscopically silent at 420 nm. The inhibition of exciton−Mn energy transfer process by the hole trapping allows a fraction of nanocrystals to avoid the depopulation of the electron in conduction band occurring *via* exciton−Mn energy transfer. Therefore, the fraction of Mn-doped nanocrystals undergoing hole trapping will exhibit the similarly slow bleach recovery dynamics as the undoped nanocrystals unless doping introduces an additional electron trap. In this case, the relative amplitudes of the fast and slow

bleach recovery represent the branching ratio between the energy transfer and hole trapping.

The inhibition of exciton−Mn energy transfer process by the charge carrier trapping can be understood from the large reduction in the wave function overlap between the donor and acceptor upon the trapping of the charge carrier if the exchange coupling of exciton and Mn^{2+} ion mediates the energy transfer.[5,24,31] According to Dexter's theory of energy transfer mediated by exchange coupling, the probability of energy transfer (P) is proportional to the coulomb interaction of two charge clouds $Q'(r_1)$ and $Q(r_2)$ in the following way.[32]

$$P \propto \left| \int Q'(r_1) \frac{1}{r_{12}} Q(r_2)\, dr_1\, dr_2 \right|^2 \int F_d(E)\, F_a(E)\, dE$$

$$Q'(r_1) = \psi^*_{exciton}(r_1)\, \psi_{Mn(excited)}(r_1),$$
$$Q(r_2) = \psi^*_{Mn(ground)}(r_2) \quad (1)$$

Here, $\psi_{exciton}$, $\psi_{Mn(excited)}$, and $\psi_{Mn(ground)}$ represent the wave functions of exciton and the excited and ground states of Mn^{2+} ion, respectively. $F_d(E)$ and $F_a(E)$ are the normalized emission and absorption spectra of donor (exciton) and acceptor (Mn^{2+} ion). Therefore, the large reduction in $Q'(r_1)$ from the trapping of charge carriers will greatly diminish the rate of the energy transfer.

In principle, both the electron trapping and hole trapping can inhibit exciton−Mn energy transfer. We concluded that hole trapping is the major process inhibiting the energy transfer for the following reason. In undoped nanocrystals, electron trapping time should be longer than the bleach recovery time probed at the band-edge (~ns) that reflects the depopulation of electron in conduction band *via* both radiative and nonradiative pathways.[20] If the electron trapping in Mn-doped nanocrystals is similar to undoped nanocrystals as indicated by the insensitivity of τ_3 on doping concentration, it will be too slow to compete with the energy transfer process that is orders of magnitude faster. Furthermore, if the electron trapping contributes significantly to the inhibition of the energy transfer, it should also be reflected in the slow component of the bleach recovery (τ_3), showing the faster recovery with the increasing electron trapping. The fact that the fixed time constant of τ_3 = 1 ns can describe the slow recovery component in both undoped and doped nanocrystals regardless of the doping concentration argues against the participation of electron trapping in the inhibition of the energy transfer. A separate experiment performed in Mn-doped CdSe/ZnS nanocrystals also indicates that Mn doping does not introduce an additional electron trapping at low doping concentrations as will be discussed later in more detail. On the other hand, hole trapping is considered to occur faster than electron trapping, as suggested by a number of earlier studies, therefore capable of inhibiting exciton−Mn energy transfer.[20,21]

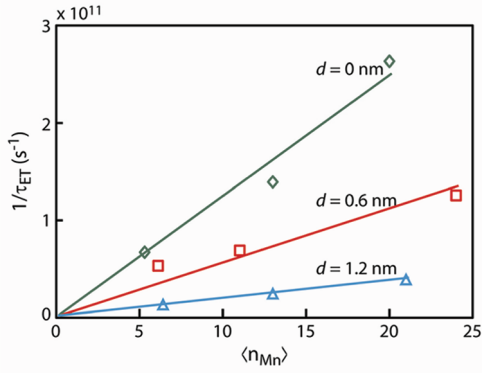

Figure 6. Doping location-dependent energy transfer rate constant ($1/\tau_{ET}$). The solid lines are trend lines assuming the energy transfer rate is linear to the average Mn doping concentration.

Furthermore, the hole trapping that inhibits exciton−Mn energy transfer process explains the observed bleach recovery dynamics very well as discussed above.

On the basis of the above argument, $r_1 + r_2$ and r_3 in Table 2 can be interpreted as the relative efficiency (or branching ratio) of exciton−Mn energy transfer (f_{ET}) and hole trapping (f_{tr}) processes, respectively. Since the time scale of the fast recovery is 1−2 orders of magnitude faster than the bleach recovery in undoped nanocrystals, we can readily assign the fast recovery component almost exclusively to exciton−Mn energy transfer provided that there is no additional electron trapping. Under this condition, the hole trapping time (τ_{tr}) can be obtained from the relative hole trapping efficiency (f_{tr}) and energy transfer time (τ_{ET}) *via* $f_{tr} = \tau_{tr}^{-1}/(\tau_{tr}^{-1} + \tau_{ET}^{-1})$, where τ_{avg} is taken as τ_{ET}. The average hole trapping time at each doping location is $\langle\tau_{tr}\rangle \approx$ 50, 80, and 100 ps for d = 0, 0.6, and 1.2 nm, respectively.

It is interesting to note the differences in the role of hole trapping in the energy transfer in Mn-doped nanocrystals and quantum dot−dye FRET pairs. In quantum dot−dye FRET pairs, the energy transfer between quantum dot and dye molecules adsorbed on the surface is of the Förster-type mediated by the dipole coupling of donor and acceptor. The hole-trapped excitons are believed to participate in the quantum dot−dye energy transfer process.[33] On the contrary, hole trapping in Mn-doped nanocrystals seems to be very effectively inhibiting the energy transfer. However, the energy transfer in Mn-doped CdS/ZnS nanocrystals can readily outcompete the hole trapping by an order of magnitude and can exhibit a very high quantum yield of Mn luminescence (Φ_{Mn}) as shown in Table 1.

In Figure 6, the rate constant ($1/\tau_{ET}$) of the energy transfer process obtained from the exponential fitting of ΔOD data is shown for all Mn-doped nanocrystals as a function of both the doping location and concentration. Two clear trends are observed. With increasing

doping concentration, $1/\tau_{ET}$ increases linearly for all the Mn-doped nanocrystals of different doping location, indicating that each Mn^{2+} ion has approximately an equal contribution as the energy acceptor at a given radial doping location. When the radial doping location is varied, the slope of the lines in Figure 6 increases rapidly as the dopant ions get closer to the center of the nanocrystals. With 1.2 nm change in the radial doping location, the rate of the energy transfer varies by 6 fold. We attempted to fit the donor−acceptor distance (R_{DA}) dependence of the energy transfer rate (k_{ET}) to the Dexter energy transfer model eq 2[32] using the slopes in Figure 6, although we have a limited number of data points.

$$k_{ET} \propto \exp(-2R_{DA}/L) \quad (2)$$

The value of L that represents the sum of van der Waals radii of donor and acceptor obtained from the fit is 1.4 nm, which is significantly smaller than the radius of CdS core (1.8 nm) and exciton Bohr radius in CdS (2.8 nm).[34] However, the largely different conduction (~1 eV) and valence (~0.2 eV) band offset in CdS/ZnS core/shell, giving rise to the different spatial extent of electron and hole wave function, makes it less straightforward to apply eq 2 to describe the distance dependence of the energy transfer rate. A further study will be needed to address this issue more quantitatively.

Since the energy transfer observed in Mn-doped CdS/ZnS nanocrystals is much faster than other radiative and nonradiative exciton relaxation pathways, the quantum yield of Mn luminescence can be quite high. In fact, all Mn-doped nanocrystals studied here exhibit a higher Mn luminescence quantum yield (Φ_{Mn}) than exciton luminescence quantum yield (Φ_{ex}) of undoped nanocrystals. The large luminescence quantum yield of Mn-doped nanocrystals is also partly due to the dominating radiative relaxation of the Mn excited state. Mn luminescence quantum yield (Φ_{Mn}) can be expressed as $\Phi_{Mn} = f_{ET} \times \phi_{Mn}$, where f_{ET} and ϕ_{Mn} are the efficiency of the energy transfer and quantum yield of the radiative relaxation of Mn, respectively. ϕ_{Mn} calculated from the measured values of Φ_{Mn} and f_{ET} is also shown in Table 1. It is interesting to note that ϕ_{Mn} decreases with decreasing τ_{Mn} and that it is as high as 0.95 in sample **b1** that has the longest Mn luminescence lifetime (τ_{Mn} = 6 ms). Although the dependence of the radiative lifetime of Mn excited state ($\tau_{Mn,r}$) on the doping location and concentration is unknown in our study, we calculated $\tau_{Mn}/\tau_{Mn,r}$ and compared with ϕ_{Mn} in Table 1 assuming that $\tau_{Mn,r}$ = 6.3 ms and independent of the doping location and concentration.[35] The values of $\tau_{Mn}/\tau_{Mn,r}$ are very close to the experimentally determined ϕ_{Mn} for most of the samples, suggesting that the variation of τ_{Mn} reflects largely the change of ϕ_{Mn} with varying doping location and concentration. The generally decreasing ϕ_{Mn} with increasing doping concentration observed in this study can be ascribed to the increasing Mn−Mn antiferromagnetic interaction at shorter interdopant distance that can enhance the nonradiative relaxation of Mn.[36,37] These observations clearly indicate that the doping location and concentration not only determine the rate of exciton−Mn energy transfer but also influences the radiative quantum yield of dopant ions. These results also provide a much clearer picture of the sensitization of Mn phosphorescence in Mn-doped nanocrystals than the earlier study solely based on the quantum yield measurement.[16]

TABLE 3. Multiexponential Fitting Parameters of ΔOD Data Probed at 880 nm to $\Sigma r_i \exp(-t/\tau_i)$

sample	r_1	r_2	r_3[a]	τ_1 (ps)	τ_2 (ps)	τ_{avg} (ps)[b]
a1	0.37	0.41	0.22	2.4	35	20
a2	0.51	0.34	0.15	1.6	21	9.4
a3	0.52	0.28	0.20	1.3	15	6.0
b1	0.32	0.44	0.24	6.8	42	27
b2	0.30	0.53	0.17	3.0	29	20
b3	0.53	0.35	0.12	3.0	27	12
c1	0.23	0.31	0.46	20	148	92
c2	0.23	0.35	0.42	13	79	53
c3	0.28	0.45	0.27	6.4	48	32

[a] r_3 is the amplitudes for τ_3 fixed at 1.3 ns. [b] $\tau_{avg} = (r_1\tau_1 + r_2\tau_2)/(r_1 + r_2)$.

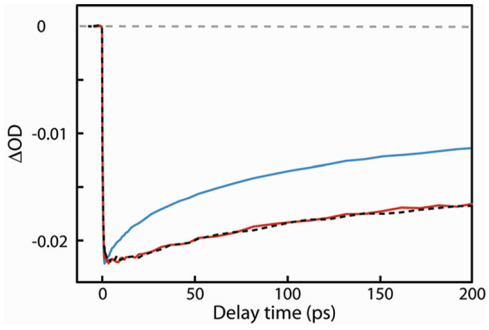

Figure 7. Bleach recovery of CdSe/ZnS nanocrystals at 590 nm. Undoped (black, dashed) and Mn-doped with $\langle n_{Mn} \rangle$ = 2.3 (red), 40 (cyan).

Now we turn to the induced absorption data probed at 880 nm. As shown in Figure 5, the decay of the induced absorption at 880 nm exhibits very similar dynamics to the bleach recovery probed at 420 nm. The parameters from the multiexponential fitting of the data are summarized in Table 3. The same kinetic scheme employed to interpret the bleach recovery data describes the dynamics of the data obtained at 880 nm. The fast decay component is ascribed to the depopulation of electron by the energy transfer. The slow decay component reflects the depopulation of electron in hole-trapped nanocrystals that do not experience the energy transfer. On the other hand, the time scales of the fast component (τ_{avg}) in 880 nm data are somewhat longer and the relative amplitudes

of the slow component (r_3) are larger than in 420 nm data. These small differences may partially be due to the potentially different effect of the hole trapping on the absorption cross sections of the interband and electron intraband transitions in Mn-doped nanocrystals. Besides these differences, the induced absorption probed at 880 nm essentially carries the same information as the bleach recovery data in our study. However, it is worth noting that the induced absorption probed at the near-infrared region can be used to study the exciton dynamics at relatively high exciton densities, where the bleach recovery at the band-edge cannot access. This is because the amplitude of the induced absorption scales roughly linearly with the initial photoexcited exciton densities, whereas the bleach recovery rapidly saturates.[24,29]

To examine whether doping of Mn introduces an additional electron trap, we compared the bleach recovery data at the band-edge in undoped and Mn-doped CdSe/ZnS nanocrystals that do not exhibit exciton−Mn energy transfer. The diameters of CdSe core and CdSe/ZnS core/shell are 5.2 and 6.1 nm, respectively. In this host nanocrystal, the energy transfer process is blocked since the bandgap of the host (λ = 590 nm) is smaller than the energy of accepting ligand field transition on Mn^{2+} ions.[23] According to the excitation spectra of Mn-doped ZnS nanocrystals studied earlier, the lowest ligand field transition ($^6A_1 \rightarrow {}^4T_1$) was centered around 520 nm, while emission ($^4T_1 \rightarrow {}^6A_1$) occurred at 590 nm. The large Stokes shift was ascribed to the strong coupling of the ligand field transition to LO phonon mode of the host matrix with a Huang−Rhys factor of ~3, which also accounts for the broad width of Mn luminescence.[38]

Figure 7 shows the bleach recovery data of undoped and Mn-doped CdSe/ZnS nanocrystals with $\langle n_{Mn} \rangle$ = 2.3 and 40 at d = 0 nm pumped at 395 nm and probed at 590 nm. The bleach recovery dynamics of the undoped and Mn-doped nanocrystals with $\langle n_{Mn} \rangle$ = 2.3 are virtually identical, indicating that doping Mn^{2+} ions does not introduce an additional electron trapping at a low doping concentration. In addition, the similar photoluminescence quantum yield of undoped (Φ_{ex} = 0.22) and Mn-doped (Φ_{ex} = 0.21) CdSe/ZnS nanocrystals also indicates that Mn doping at low densities does not introduce an additional charge carrier trapping that leads to the nonradiative relaxation of excitons. While CdSe was used as the core instead of CdS to prevent the energy transfer, the evidence for the absence of an additional electron trapping in CdSe is consistent with the insensitivity of τ_3 to Mn doping in the CdS/ZnS host that is also indicative of the absence of the additional electron trapping. However, at much higher doping concentrations, for example, $\langle n_{Mn} \rangle$ = 40, the bleach signal begins to show faster recovery and the quantum yield of exciton luminescence decreases. This observation suggests that significantly more additional charge carrier traps can be created including electron traps at very high doping concentrations, perhaps due to the creation of a structural defect.

In conclusion, doping location-dependent dynamics of exciton relaxation and energy transfer in Mn-doped CdS/ZnS nanocrystals are investigated *via* transient absorption measurements. By using the doping location- and concentration-controlled nanocrystals that removed a major structural heterogeneity, previously unavailable information on the dynamics of energy transfer and competing hole trapping is obtained. The rate of exciton−Mn energy transfer exhibited a strong dependence on the doping radius for a given doping concentration and occurred on the time scales of a few to tens of picoseconds within the range of the doping concentration of this study. In the competition between exciton−Mn energy transfer and charge carrier trapping that inhibits the energy transfer, hole trapping was identified as the major process competing with exciton−Mn energy transfer. Due to the fast energy transfer that efficiently competes with nonradiative relaxation pathways, Mn-doped nanocrystals exhibited much higher luminescence quantum yield than undoped nanocrystals. Knowledge on the structurally resolved dynamics of various photophysical processes in Mn-doped nanocrystals obtained in this study will provide a valuable insight into the structural control of the properties of doped semiconductor nanocrystals.

METHODS

Synthesis of Nanocrystals. The undoped and Mn-doped CdS/ZnS or CdSe/ZnS core/shell nanocrystals were prepared using the layer-by-layer coating and doping methods following the published procedures with some modifications.[18,39,40] CdS nanocrystals were synthesized by injecting 1-octadecene (ODE) solution of sulfur (0.25 M, 2.0 mL) to the mixture of cadmium oxide (0.126 g), oleic acid (2.02 g), and ODE (12.0 mL) heated at 250 °C under nitrogen atmosphere. After the injection, the growth temperature was dropped to 240 °C. The nanocrystals were precipitated with acetone after cooling to room temperature. The precipitate was further rinsed twice by dissolving and precipitating with toluene and methanol. CdSe nanocrystals were prepared by injecting the tributylphosphine solution of selenium (10% w/w, 0.80 g) to the mixture of cadmium oxide (0.250 g), hexadecylamine (2.85 g), trioctylphosphine oxide (1.15 g), tetradecylphosphonic acid (1.09 g), and tributylphosphine (1.00 g) at 295 °C under nitrogen atmosphere. Subsequently, the growth temperature was lowered to 275 °C. After reaching the desired nanocrystal diameter, the solution was cooled to 60 °C and a mixture of octanoic acid and toluene (~7 mL each) was added. The precipitated CdSe nanocrystals were rinsed by the repeated dispersion and precipitation using toluene and methanol, respectively.

To dope Mn^{2+} ions on the surface of CdS nanocrystals (d = 0 nm), an oleylamine (OAm) solution of manganese diethyldithiocarbamate was added to the CdS nanocrystals in ODE and

OAm at 220 °C and cooled to room temperature after 20 min. For the Mn^{2+} ions doped in ZnS (d = 0.6 and 1.2 nm), an ODE solution of sulfur and OAm solution of manganese acetate were added to the CdS/ZnS nanocrystals in ODE and OAm at 260 °C. The solution was cooled to room temperature after 20 min.[18] The cleaning procedure is the same as that of CdS nanocrystals. After cleaning the nanocrystals, an extra ZnS shell was coated to ensure that the Mn^{2+} ions are embedded in the nanocrystals. To coat an extra ZnS shell on the surface of Mn-doped or undoped nanocrystals, the mixture of the nanocrystals, OAm, and ODE were initially heated to 220 °C under nitrogen atmosphere followed by the addition of an ODE solution of sulfur and zinc stearate alternately during a 10 min interval. The cleaning procedure is also the same as that of CdS nanocrystals.

Quantum Yield Measurement. The luminescence quantum yields of exciton (Φ_{ex}) and Mn (Φ_{Mn}) in undoped and Mn-doped nanocrystals were measured using either standard dye or CdSe/ZnS nanocrystals of known quantum yield as the reference material. In all the measurements, hexane was used as the solvent for the nanocrystals, and 370 nm light from a xenon lamp was used as the excitation source. Φ_{ex} of both undoped and Mn-doped CdS/ZnS nanocrystals was measured using quinine sulfate in 1.0 N aqueous H_2SO_4 solution (quantum yield = 0.546)[41] as the reference dye. For the measurement of Φ_{Mn}, undoped CdSe/ZnS nanocrystals emitting at 600 nm were used as the reference material since no organic dye has sufficiently large Stokes shift that matches the absorption and emission spectra of Mn-doped nanocrystals.[7] The quantum yield of undoped CdSe/ZnS reference nanocrystals was measured using rhodamine 101 dissolved in ethanol under nitrogen atmosphere (quantum yield = 1.00) with excitation at 550 nm.[42] To confirm the validity of the quantum yield of the reference dyes, the quantum yields of the quinine sulfate and rhodamine 101 were cross-checked with coumarin 1 and cresyl violet, respectively. The quantum yield of coumarin 1 in a 1:1 mixture of ethanol and water and cresyl violet in methanol obtained using quinine sulfate and rhodamine 101 as reference is within 3% from the reported values, 0.30 and 0.66−0.67, respectively.[43,44] All the measurements were reproduced with less than 5% error.

Time-Dependent Mn Luminescence Intensity Measurement. The time-dependent Mn luminescence intensity was measured by exciting the Mn-doped nanocrystals dispersed in hexane with a pulsed nitrogen laser (pulse duration <3 ns, wavelength 337 nm). The Mn luminescence was selected by a monochromator, detected by a photomultiplier tube, and the signal was collected by a digital oscilloscope. Each time-dependent luminescence curve was fit to a two exponential function, and the averaged lifetime (τ_{Mn}) was calculated using eq 3, where a_1 and a_2 are the amplitude and t_1 and t_2 are the time constants of the two-exponential fit.[45]

$$\tau_{Mn} = (a_1 t_1^2 + a_2 t_2^2)/(a_1 t_1 + a_2 t_2) \quad (3)$$

Transient Absorption Measurement. The pump pulse at 395 nm was generated by the frequency doubling of 790 nm output from a Ti:sapphire laser in a β-barium borate crystal at 3 kHz repetition rate. The pulse width and fwhm beam diameter of the pump beam were 70 fs and 300 μm, respectively. At the pump intensity of this study, the average density of photoexcited exciton is less than 0.5. A white light continuum generated in 1 mm-thick CaF_2 and a sapphire window by focusing a 790 nm beam was used as the probe light (fwhm beam diameter $\approx$ 30 μm) at the band-edge (420 nm) and near-infrared (880 nm) regions, respectively. When CaF_2 was used, the window was translated rapidly to obtain the stable continuum probe light. The hexane solutions of the sample nanocrystals were circulated in a 1 mm-thick quartz liquid cell at the linear flow rate of ~1 m/s to avoid potential photodamage and reexcitation of the same sample area. Fast circulation is particularly important for Mn-doped nanocrystals since the lifetime of a Mn excited ligand field state is several milliseconds. The nanocrystal concentrations of all the samples were kept the same at ~6.4 μM.

Acknowledgment. This work was supported by the Welch Foundation (Grant No. A-1639). We thank the Microscopy and Imaging Center, Material Characterization Facility, and Elemental Analysis Laboratory of Texas A&M University for TEM, UV−vis spectra, and ICP−MS measurements.

Supporting Information Available: Time-dependent Mn luminescence data, discussion on the determination of the radial doping location, transient absorption data and the fits. This material is available free of charge *via* the Internet at http://pubs.acs.org.

REFERENCES AND NOTES

1. Norris, D. J.; Efros, A. L.; Erwin, S. C. Doped Nanocrystals. *Science* **2008**, *319*, 1776–1779.
2. Beaulac, R.; Archer, P. I.; Ochsenbein, S. T.; Gamelin, D. R. Mn^{2+}-Doped CdSe Quantum Dots: New Inorganic Materials for Spin-Electronics and Spin-Photonics. *Adv. Funct. Mater.* **2008**, *18*, 3873–3891.
3. Mocatta, D.; Cohen, G.; Schattner, J.; Millo, O.; Rabani, E.; Banin, U. Heavily Doped Semiconductor Nanocrystal Quantum Dots. *Science* **2011**, *332*, 77–81.
4. Ochsenbein, S. T.; Gamelin, D. R. Quantum Oscillations in Magnetically Doped Colloidal Nanocrystals. *Nat. Nanotechnol.* **2011**, *6*, 112–115.
5. Beaulac, R.; Ochsenbein, S.; Gamelin, D. Colloidal Transition-Metal-Doped Quantum Dots. In *Nanocrystal Quantum Dots*, 2nd ed.; Klimov, V. I., Ed.; CRC Press: Boca Raton, FL, 2010; pp 397−453.
6. Yu, J. H.; Liu, X.; Kweon, K. E.; Joo, J.; Park, J.; Ko, K. T.; Lee, D. W.; Son, J. S.; Park, J.; Kim, Y.-W.; Hwang, G. S.; Dobrowolska, M.; Furdyna, J. K.; Hyun, T. Giant Zeeman Splitting in Nucleation Controlled Doped CdSe:Mn^{2+} Quantum Nanoribbons. *Nat. Mater.* **2010**, *9*, 47–53.
7. Wood, V.; Halpert, J. E.; Panzer, M. J.; Bawendi, M. G.; Bulović, V. Alternating Current Driven Electroluminescence from ZnSe/ZnS:Mn/ZnS Nanocrystals. *Nano Lett.* **2009**, *9*, 2367–2371.
8. Beaulac, R.; Schneider, L.; Archer, P. I.; Bacher, G.; Gamelin, D. R. Light-Induced Spontaneous Magnetization in Doped Colloidal Quantum Dots. *Science* **2009**, *325*, 973–976.
9. Magana, D.; Perera, S. C.; Harter, A. G.; Dalal, N. S.; Strouse, G. F. Switching-on Superparamagnetism in Mn/CdSe Quantum Dots. *J. Am. Chem. Soc.* **2006**, *128*, 2931–2939.
10. Lee, S.; Dobrowolska, M.; Furdyna, J. K. Zeeman Mapping of Exciton Localization in Self-Assembled CdSe Quantum Dots Using Diluted Magnetic Semiconductors. *Solid State Commun.* **2007**, *141*, 311–315.
11. Seufert, J.; Bacher, G.; Scheibner, M.; Forchel, A.; Lee, S.; Dobrowolska, M.; Furdyna, J. K. Dynamical Spin Response in Semimagnetic Quantum Dots. *Phys. Rev. Lett.* **2001**, *88*, 027402.
12. Jones, M.; Lo, S. S.; Scholes, G. D. Quantitative Modeling of the Role of Surface Traps in CdSe/CdS/ZnS Nanocrystal Photoluminescence Decay Dynamics. *Proc. Natl. Acad. Sci.* **2009**, *106*, 3011–3016.
13. Norris, D. J.; Yao, N.; Charnock, F. T.; Kennedy, T. A. High-Quality Manganese-Doped ZnSe Nanocrystals. *Nano Lett.* **2001**, *1*, 3–7.
14. Chen, D.; Viswanatha, R.; Ong, G. L.; Xie, R.; Balasubramaninan, M.; Peng, X. Temperature Dependence of "Elementary Processes" in Doping Semiconductor Nanocrystals. *J. Am. Chem. Soc.* **2009**, *131*, 9333–9339.
15. Mikulec, F. V.; Kuno, M.; Bennati, M.; Hall, D. A.; Griffin, R. G.; Bawendi, M. G. Organometallic Synthesis and Spectroscopic Characterization of Manganese-Doped CdSe Nanocrystals. *J. Am. Chem. Soc.* **2000**, *122*, 2532–2540.
16. Yang, Y.; Chen, O.; Angerhofer, A.; Cao, Y. C. Radial-Position-Controlled Doping of CdS/ZnS Core/Shell Nanocrystals: Surface Effects and Position-Dependent Properties. *Chem.—Eur. J.* **2009**, *15*, 3186–3197.
17. Ithurria, S.; Guyot-Sionnest, P.; Mahler, B.; Dubertret, B. Mn^{2+} as a Radial Pressure Gauge in Colloidal Core/Shell Nanocrystals. *Phys. Rev. Lett.* **2007**, *99*, 265501.
18. Yang, Y.; Chen, O.; Angerhofer, A.; Cao, Y. C. On Doping CdS/ZnS Core/Shell Nanocrystals with Mn. *J. Am. Chem. Soc.* **2008**, *130*, 15649–15661.

19. Klimov, V. I.; Schwarz, C. J.; McBranch, D. W.; Leatherdale, C. A.; Bawendi, M. G. Ultrafast Dynamics of Inter- and Intraband Transitions in Semiconductor Nanocrystals: Implications for Quantum-Dot Lasers. *Phys. Rev. B* **1999**, *60*, R2177–R2180.
20. Knowles, K. E.; McArthur, E. A.; Weiss, E. A. A Multi-Timescale Map of Radiative and Nonradiative Decay Pathways for Excitons in CdSe Quantum Dots. *ACS Nano* **2011**, *5*, 2026–2035.
21. Sewall, S. L.; Cooney, R. R.; Anderson, K. E. H.; Dias, E. A.; Sagar, D. M.; Kambhampati, P. State-Resolved Studies of Biexcitons and Surface Trapping Dynamics in Semiconductor Quantum Dots. *J. Chem. Phys.* **2008**, *129*, 084701.
22. Underwood, D. F.; Kippeny, T.; Rosenthal, S. J. Ultrafast Carrier Dynamics in CdSe Nanocrystals Determined by Femtosecond Fluorescence Upconversion Spectroscopy. *J. Phys. Chem. B* **2001**, *105*, 436–443.
23. Beaulac, R.; Archer, P. I.; van Rijssel, J.; Meijerink, A.; Gamelin, D. R. Exciton Storage by Mn^{2+} in Colloidal Mn^{2+}-Doped CdSe Quantum Dots. *Nano Lett.* **2008**, *8*, 2949–2953.
24. Chen, H.-Y.; Chen, T.-Y.; Son, D. H. Measurement of Energy Transfer Time in Colloidal Mn-Doped Semiconductor Nanocrystals. *J. Phys. Chem. C* **2010**, *114*, 4418–4423.
25. Bol, A. A.; Meijerink, A. Long-Lived Mn^{2+} Emission in Nanocrystalline ZnS:Mn^2. *Phys. Rev. B* **1998**, *58*, R15997–R16000.
26. Pandey, A.; Guyot-Sionnest, P. Slow Electron Cooling in Colloidal Quantum Dots. *Science* **2008**, *322*, 929–932.
27. Boulesbaa, A.; Huang, Z.; Wu, D.; Lian, T. Competition between Energy and Electron Transfer from CdSe QDs to Adsorbed Rhodamine B. *J. Phys. Chem. C* **2010**, *114*, 962–969.
28. Klimov, V. I. Spectral and Dynamical Properties of Multiexcitons in Semiconductor Nanocrystals. *Annu. Rev. Phys. Chem.* **2007**, *58*, 635–673.
29. Ueda, A.; Tayagaki, T.; Kanemitsu, Y. Dynamics of Quantized Auger Recombination in CdSe Nanocrystals Studied by Femtosecond Intraband Pump–Probe Spectroscopy. *J. Phys. Soc. Jpn.* **2009**, *78*, 083706.
30. Burda, C.; Link, S.; Mohamed, M.; El-Sayed, M. The Pump Power Dependence of the Femtosecond Relaxation of CdSe Nanoparticles Observed in the Spectral Range from Visible to Infrared. *J. Chem. Phys.* **2002**, *116*, 3828–3833.
31. The exact exciton–Mn energy transfer mechanism in Mn-doped nanocrystals is still under debate.
32. Dexter, D. L. A Theory of Sensitized Luminescence in Solids. *J. Chem. Phys.* **1953**, *21*, 836–850.
33. Dayal, S.; Burda, C. Surface Effects on Quantum Dot-Based Energy Transfer. *J. Am. Chem. Soc.* **2007**, *129*, 7977–7981.
34. Gaponenko, S. V. *Optical Properties of Semiconductor Nanocrystals*; Cambridge University Press: Cambridge, 1999.
35. The hypothetical $\tau_{Mn,r}$ was obtained using the eqation $\phi_{Mn} = \tau_{Mn}/\tau_{Mn,r}$ and parameters from the sample with highest quantum yield (**b1**), that is, ϕ_{Mn} and $\tau_{Mn} = 0.95$ and 6.0 ms, respectively.
36. Suyver, J. F.; Wuister, S. F.; Kelly, J. J.; Meijerink, A. Luminescence of Nanocrystalline ZnSe:Mn^2. *Phys. Chem. Chem. Phys.* **2000**, *2*, 5445–5448.
37. Vink, A. P.; Bruin, M. A. d.; Roke, S.; Peijzel, P. S.; Meijerink, A. Luminescence of Exchange Coupled Pairs of Transition Metal Ions. *J. Electrochem. Soc.* **2001**, *148*, E313–E320.
38. Chen, W.; Sammynaiken, R.; Huang, Y.; Malm, J.-O.; Wallenberg, R.; Bovin, J.-O.; Zwiller, V.; Kotov, N. A. Crystal Field, Phonon Coupling and Emission Shift of Mn^{2+} in ZnS:Mn Nanoparticles. *J. Appl. Phys.* **2001**, *89*, 1120–1129.
39. Yu, W. W.; Peng, X. Formation of High-Quality CdS and Other II–VI Semiconductor Nanocrystals in Noncoordinating Solvents: Tunable Reactivity of Monomers. *Angew. Chem., Int. Ed.* **2002**, *41*, 2368–2371.
40. Peng, Z. A.; Peng, X. Formation of High-Quality CdTe, CdSe, and CdS Nanocrystals Using CdO as Precursor. *J. Am. Chem. Soc.* **2000**, *123*, 183–184.
41. Melhuish, W. H. Quantum Efficiencies of Fluorescence of Organic Substances: Effect of Solvent and Concentration of the Fluorescent Solute. *J. Phys. Chem.* **1961**, *65*, 229–235.
42. Karstens, T.; Kobs, K. Rhodamine B and Rhodamine 101 as Reference Substances for Fluorescence Quantum Yield Measurements. *J. Phys. Chem.* **1980**, *84*, 1871–1872.
43. Jones, G.; Jackson, W. R.; Choi, C. Y.; Bergmark, W. R. Solvent Effects on Emission Yield and Lifetime for Coumarin Laser Dyes. Requirements for a Rotatory Decay Mechanism. *J. Phys. Chem.* **1985**, *89*, 294–300.
44. Isak, S. J.; Eyring, E. M. Fluorescence Quantum Yield of Cresyl Violet in Methanol and Water as a Function of Concentration. *J. Phys. Chem.* **1992**, *96*, 1738–1742.
45. Lakowicz, J. R. *Principles of Fluorescence Spectroscopy*. 3rd ed.; Springer: New York, 2006.